



A hierarchically honeycomb-like carbon via one-step surface and pore adjustment with superior capacity for lithium–oxygen batteries

Jing Li ^{a,b}, Yining Zhang ^{a,*}, Wei Zhou ^{a,b}, Hongjiao Nie ^{a,b}, Huamin Zhang ^{a,*}

^aDivision of Energy Storage, Dalian National Laboratory for Clean Energy, Dalian Institute of Chemical Physics, Chinese Academy of Sciences, Zhongshan Road 457, Dalian 116023, China

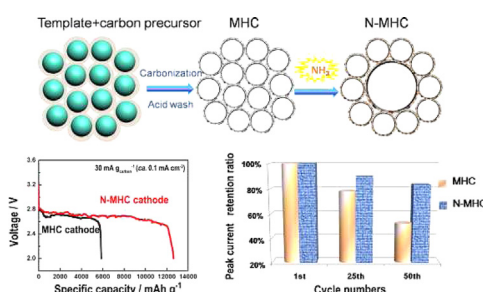
^bUniversity of Chinese Academy of Sciences, Beijing 100039, China



HIGHLIGHTS

- Novel nitrogen-doped hierarchical porous carbon for cathode of Li–O₂ battery.
- Pore optimization and surface nitrogenation by one-step ammonia activation.
- Superior discharge capacity of 12,600 mAh g⁻¹, 4 times that of commercial carbon.
- Enhanced activity for oxygen reduction and cycling stability.

GRAPHICAL ABSTRACT



ARTICLE INFO

Article history:

Received 6 January 2014

Received in revised form

5 March 2014

Accepted 24 March 2014

Available online 1 April 2014

Keywords:

Lithium–oxygen battery

Cathode

Hierarchical porous structure

Ammonia activation

Electrochemistry

Oxygen reduction

ABSTRACT

Li–O₂ batteries have attracted considerable attention due to their high energy density. The critical challenges that limit the practical applications include effective utilization of electrode space for solid products deposition and acceptable cycling performance. In the present work, a nitrogen-doped micron-sized honeycomb-like carbon is developed for use as a cathode material for Li–O₂ batteries. This novel material is obtained by using nano-CaCO₃ particles as hard template and sucrose as the carbon source, followed by thermal annealing at 800 °C in ammonia. With one-step ammonia activation, surface nitrogenation and further pore structure optimization are realized simultaneously. The material exhibits enhanced activity for oxygen reduction reaction and oxygen transfer ability. Surprisingly, an improved cycling stability is also obtained. As a result, a superior discharge capacity up to 12,600 mAh g⁻¹ is achieved, about 4 times that of commercial Ketjenblack carbon. The results provide a novel route to construct effective non-metal carbon-based cathodes for high performance of Li–O₂ batteries.

© 2014 Elsevier B.V. All rights reserved.

1. Introduction

Electrochemical energy storage is of great importance due to its promising potential as a power system for future

transportations. Among various energy storage technologies, Li–O₂ batteries (LOBs) have received great attention with extremely high theoretical energy density up to 3212 Wh kg⁻¹ (O₂ included), 5–10 fold higher relative to the state-of-the-art lithium-ion batteries [1–3].

Actually, the practical energy density that LOBs can achieve is related to the capacity, which is mainly determined by the cathode. In a typical discharge process, the cathode pore supplies room for the insoluble Li₂O₂ product deposition. Therefore, the electrode

* Corresponding authors. Tel.: +86 411 84379072; fax: +86 411 84665057.

E-mail addresses: zhangyn@dicp.ac.cn (Y. Zhang), zhanghm@dicp.ac.cn (H. Zhang).

pore structure design plays a key role on the cell performance. Specifically, the discharge performance depends on the cathode pore volume, of which the mesopore volume has a large contribution [4,5]. Tran et al. [6] proposed a model mechanism based on gas diffusion electrode and showed that small pores were passivated by the reaction products blocking and thus preventing them from further utilization. As a consequence, high volume of ultra-large mesopores is preferred to accommodate more discharge products [7]. Moreover, the pores meanwhile function as the oxygen transport way, and the Li_2O_2 precipitation would block the oxygen pathway. Thus, how to make sure of an efficient O_2 transport in the electrode is essential to the better use of the electrode space. One effective strategy is to construct the “oxygen highways” by 3-dimensional (3D) interconnected network of electrodes pores [8–11]. With hierarchically porous architectures, functionalized graphene sheets displayed super high capacity (15,000 mAh g^{-1}) reported by Zhang's group [12]. Similarly, we have recently developed a micron-sized honeycomb-like carbon (MHC) which demonstrated excellent utilization of pores in LOBs ascribed to its hierarchical pore structure [13]. With intrinsic large mesopores in MHC particles themselves accommodating the solid products and micron-sized tunnels among them facilitating oxygen transport, the discharge capacity of MHC is twice of the best commercial carbon (Ketjenblack). However, the “oxygen highways” just lie in the interspace among the carbon particles. Actually, the interior oxygen transport paths in the huge particles are also in great need, and thus further pore structure optimization is worth to be done.

Besides the challenges to construct effective cathode architecture, it is highly desirable to search cost-effective cathode materials with high catalytic activities. As the electrode reaction takes place on the interface, the role that surface chemistry composition of carbon electrode plays cannot be ignored. Recently, much attention has been paid to the metal-free nitrogen-containing porous carbon for LOBs [14–17]. Nitrogen-doped materials such as carbon nanotubes and graphene nanosheets have displayed largely improved electrocatalytic activity. The improved performance is ascribed to the defects and functional groups as active sites introduced by nitrogen doping [15]. Normally, nitrogen atoms can be introduced through two approaches: either *in situ* doping method with carbonization of nitrogen-rich carbon precursors (such as polyacrylonitrile, melamine, urea-polymer), or via treatment of carbon by gaseous NH_3 or HCN [18]. NH_3 has been by far the most frequently used nitrogenation reagent. At high temperatures, NH_3 will decompose to free radicals such as $\cdot\text{NH}_2$, $\cdot\text{NH}$, which will attack the carbon material to form nitrogen-containing functional groups [19]. More importantly, apart from the surface chemical modification, nitrogenation via NH_3 at elevated temperature can also takes effect on pore structure adjustment [18]. As reported by Mangun and Wang, the pore sizes of carbon can be tuned via NH_3 activation, as the formed radicals can etch carbon fragments, leading to increased porosity [20,21].

Inspired by the two aspects above, a nitrogen-doped micron-sized honeycomb-like carbon (N-MHC) was developed through one-step ammonia activation in this work, to incorporate active nitrogen into carbon and optimize pore structure simultaneously. Based on the combined effect of surface catalysis enhancement and facilitated oxygen transport, an LOB employing the fabricated N-MHC cathode exhibited an excellent performance with a discharge capacity of 12,600 mAh g^{-1} , among the highest ever reported. In addition, the cost-effective N-MHC demonstrated good cycling stability. The results provide new insights into the high performance of non-metal carbon-based cathodes for LOBs.

2. Experimental

2.1. Synthesis of nitrogen-doped micron-sized honeycomb-like carbon (N-MHC)

The commercial nano- CaCO_3 particles (ca. 30–50 nm, Henan Keli New Material Co. Ltd) were used as hard template and sucrose (Tianjin Fuchen) as carbon precursor, as was previously reported. Firstly, sucrose (2 g) was dissolved in deionized water (15 mL), in which CaCO_3 nanoparticles (4 g) were dispersed at 60 °C under vigorous stirring until a slurry mixture was obtained. Then, the mixture was vacuum dried at 60 °C for 24 h, and the carbonization was carried out in a furnace under argon atmosphere with temperature ramping from 25 to 500 °C at 5 °C min^{-1} , 500–900 °C at 2 °C min^{-1} , and then kept at 900 °C for 5 h. Lastly, the template was removed by washing with 2 M HCl aqueous solution under stirring for 5 h, and filtered with deionized water. After vacuum drying at 80 °C for 24 h, the MHC material was obtained. Ammonia heat-treatment was performed by placing 80 mg of MHC in a quartz tubing under flowing NH_3 (~40 mL min^{-1} , purity 99.99%) with a heating ramp rate of 10 °C min^{-1} to 800 °C and kept at 800 °C for 2 h, then the N-MHC material was obtained. The weight loss during NH_3 annealing was recorded.

2.2. Cathode preparations

The cathode was prepared by a dry rolling process described in our previous work. MHC or N-MHC and PTFE (Teflon®, solid content = 61.5%, DuPont) with a weight ratio of 8:2 were mixed and rolled into a thin film. After dried at 80 °C under vacuum for over 8 h, the film was punched to disks with a diameter of 15 mm as cathodes and the carbon loadings were ~6.3 ± 0.4 mg.

2.3. Physical characterizations

Nitrogen sorption measurements were performed on ASAP 2010 (Micromeritics, USA) at 77 K to obtain pore properties such as the specific surface area, the pore size distribution (PSD), and total pore volume of MHC and N-MHC materials. The specific surface area was determined according to the Brunauer–Emmett–Teller (BET) method in the relative pressure range of 0.06–0.20. The PSDs of MHC and N-MHC were calculated from the desorption branch by the Barrett–Joyner–Halenda (BJH) method. The morphologies of prepared MHC and N-MHC electrodes were characterized by a QUANTA 200F scanning electronic microscope (SEM), operating at an acceleration voltage of 20 kV. The structural investigation of N-MHC sample was conducted by high-angle annular dark-field (HAADF)-scanning transmission electron microscopy (STEM) (FEI Tecnai G² TF20). Energy dispersive X-ray spectroscopy (EDX) analysis was performed, and the elemental mapping was conducted under STEM mode with the EDX detector as recorder. The surface chemical composition of the samples were determined by X-ray photoelectron spectroscopy (XPS) on a VG ESCALAB250 spectrometer (Thermo Electron, U.K.) using Al K α radiation operation at 300 W. Spectra were calibrated according to the C1s (284.6 eV) peak. The weight loss of MHC by NH_3 thermal annealing was recorded after 800 °C heat treatment. The pyrolysis of MHC was investigated by thermogravimetry (TG) on a Setaram Setsys 16/18 thermoanalyzer with a heating rate of 10 °C min^{-1} to 800 °C in Ar flow. Raman scattering spectra were recorded on a Renishaw inVia Raman Microscope (514 nm laser).

2.4. Electrochemical measurements

1 M lithium bis(trifluoromethanesulfonyl)imide (LiTFSI) in tetraethylene glycol dimethyl ether (TEGDME) was used as electrolyte. The water content of TEGDME solvent was strictly controlled under 10 ppm determined by Karl-Fischer titration. A polypropylene fiber separator (Novatex 2471, Freudenberg Filtration Technologies KG) (22 mm in diameter) was used as the separator. The amount of electrolyte was 100 μ L. All Li–O₂ single cells were discharged galvanostatically (ArbinBT-2000) at a rate of 30 mA g^{−1} of carbon (ca. 0.1 mA cm^{−2}) with a cut-off voltage of 2.0 V in a 1.2 atm O₂ atmosphere at 25 °C. The specific capacity of the cell was normalized by the mass of the carbon materials in the cathode.

The cyclic voltammetry (CV) tests were conducted in a three-electrode cell. A Li foil immersed into 0.5 M LiTFSI in TEGDME solution, connected to the main solution by a glass frit, was used as reference electrode. The Li foil was also used as the counter electrode. A glassy carbon disk (0.1256 cm², Pine Inc.) covered by 5 μ L of the suspension made with 1 mg MHC or N-MHC, 15 μ L lithiated Nafion® and 0.5 mL 2-propanol was used as the working electrode.

CV experiments were performed by scanning the disk potential between 2.0 V and 4.3 V (0.5 M LiTFSI in TEGDME) at a scan rate of 10 mV s^{−1}. All scans were first conducted under N₂ flow, then under O₂ before purging for 60 min. The electrochemical stability tests were obtained from 50 cycles in O₂-saturated solution. All experiments were conducted at 25 °C by using an AFCBP1 bipotentiostat (Pine Research Instrumentation, USA) controlled with Aftermath software.

3. Results and discussion

The pore structures of pristine MHC and N-MHC were investigated using N₂ adsorption–desorption isotherms as shown in Fig. 1. Both carbon materials are found to exhibit type-IV isotherms following the IUPAC classification, indicating the presence of mesopores. According to the pore size distributions (PSDs) of MHC and N-MHC in Fig. 1(b), both samples display typical dual-region distributions with dominant peaks at ca. 3 nm and 30–60 nm. It is clear that the PSD peak of the N-MHC sample is right shifted from ~30 nm to ~50 nm, which might be due to the etching effect of NH₃. Meanwhile, more large mesopores (10–50 nm) and macropores (>50 nm) called Pore A (>10 nm) are also created, and the corresponding volume increases by about 30% (Table 1). These pores are appropriate for Li₂O₂ accommodation and this change in pore structure is beneficial to improve discharge capacity. In all, the

Table 1
Pore textural properties of the prepared carbon materials.

Sample	S_{BET} [m ² g ^{−1}] ^a	V_{total} [cm ³ g ^{−1}] ^b	$V_{\text{Pore A}}$ [cm ³ g ^{−1}] ^c	$V_{\text{Pore B}}$ [cm ³ g ^{−1}] ^d
MHC	785	1.10	0.70	0.40
N-MHC	1033	1.55	1.02	0.53

^a S_{BET} : BET surface area.

^b V_{total} : total pore volume obtained from N₂ desorption isotherms at 77 K (pores ranging from 1.7 to 300.0 nm).

^c $V_{\text{Pore A}}$: volume of pores larger than 10 nm.

^d $V_{\text{Pore B}}$: volume of pores smaller than 10 nm.

total pore volume increases from 1.10 cm³ g^{−1} (MHC) to 1.55 cm³ g^{−1} (N-MHC). This result is mainly due to the increased Pore A volume, which accounts for nearly 70% of the increment of total pore volume. In addition, the BET surface area of N-MHC (1033 m² g^{−1}) is higher than that of MHC (785 m² g^{−1}).

As the electrode porosity contributes more than the carbon material itself to its discharge capacity, the morphologies characterization were carried out on the prepared electrode. According to the SEM images in Fig. 2(a) and (b), both electrodes possess honeycomb-like mesopores generated by the addition of CaCO₃ template, as well as macroporous tunnels constituted by the carbon particles interspaces [22]. In contrast, compared with MHC electrode, the N-MHC electrode possesses more loosely stacked macropores and displays highly developed porous structure in the electrode framework. More importantly, as shown in Fig. 2(c) and (d), inner macropores in carbon particles ranging from 0.5 to 1.5 μ m present for N-MHC electrode at higher magnification, while none for MHC. This further demonstrates the construction of more Pore A (>10 nm), in accordance with the PSD results.

The formation of macroporous holes inside particles of N-MHC is illustrated in Fig. 2(e) and stated as follows: First, intrinsic mesopores are constructed by nano-CaCO₃ template after washing by acid. Then, ammonia acts as an etchant and play a role of pore activation during pyrolysis process. The macropores are formed through the etching of carbon fragments by the radicals generated from the decomposition of NH₃ [21]. These macroporous network then function as “buffering room” for oxygen storage and facilitate oxygen diffusion to neighboring mesopores, where Li₂O₂ precipitations mainly take place.

The presence of nitrogen-containing groups on the surface of the carbon materials was confirmed by X-ray photoelectron spectroscopy (XPS). As shown in Fig. 3(a), a distinct N 1s peak is observed for N-MHC, confirming the incorporation of nitrogen

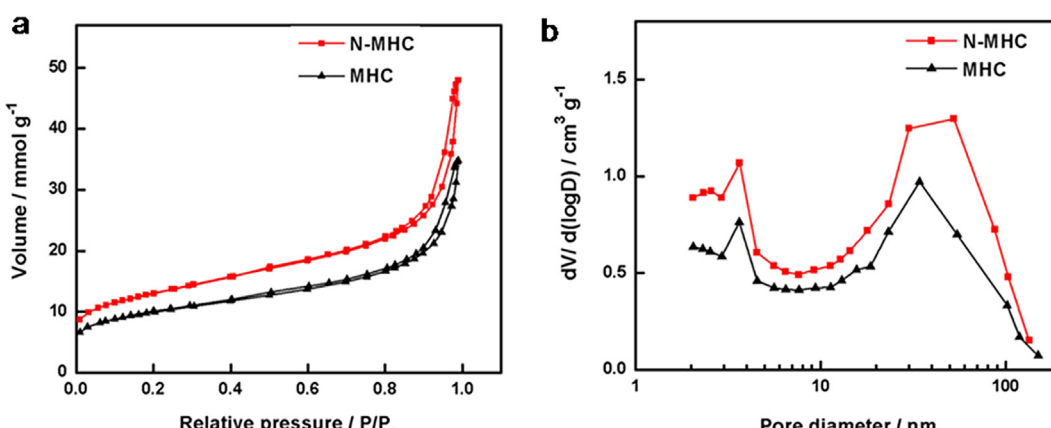


Fig. 1. (a) N₂ adsorption–desorption isotherms at 77 K for pristine MHC and NH₃ modified carbon materials (N-MHC). (b) Pore size distribution for MHC and N-MHC materials obtained by BJH (Barrett–Joyner–Halenda) method.

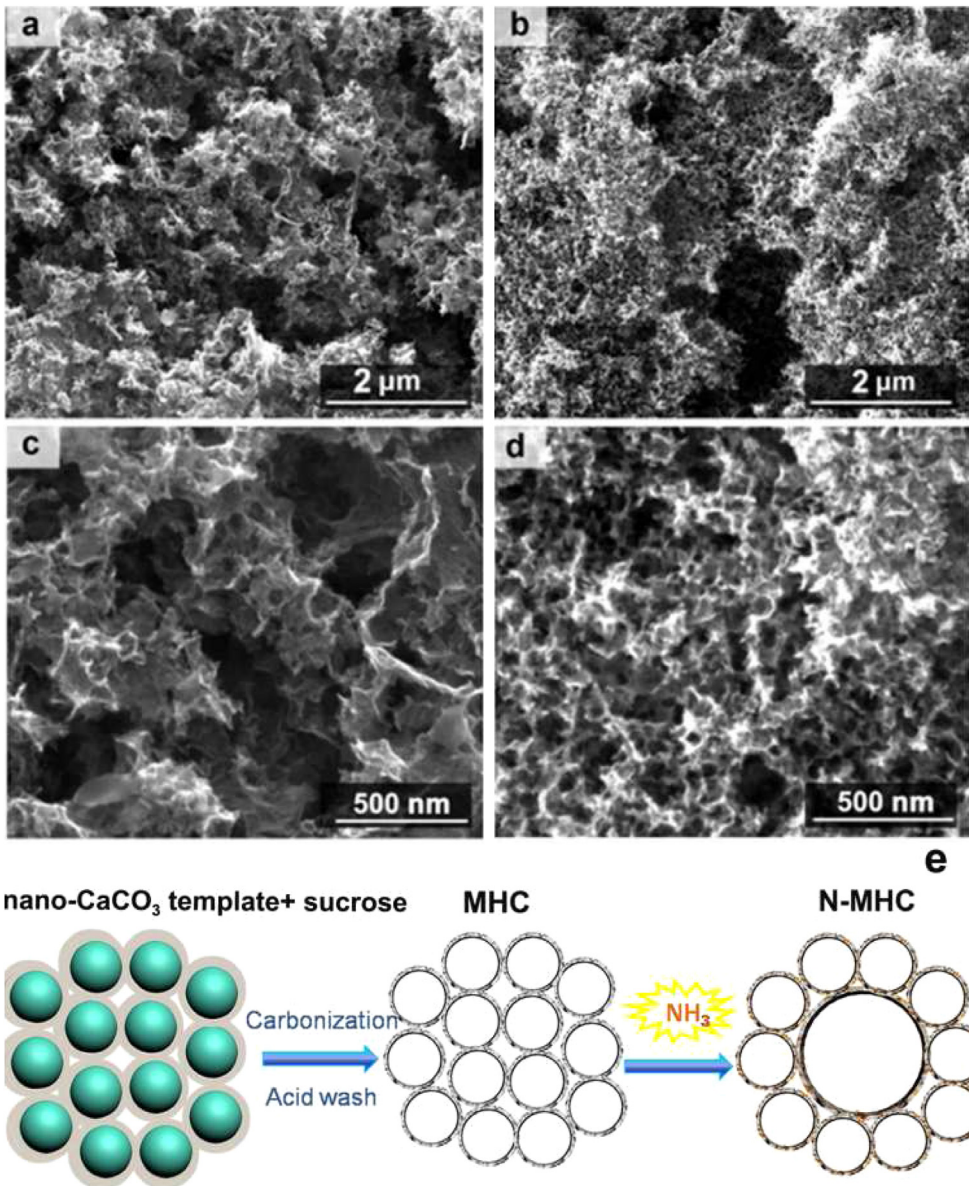


Fig. 2. (a–d) Scanning electronic microscope (SEM) images of carbon electrodes at different magnification. (a, c) N-MHC electrode; (b, d) MHC electrode. (e) An illustration of the NH₃ activation for intrinsic large holes of N-MHC.

atom into MHC structure. The nitrogen doping level of 3.58 at.% is detected for N-MHC. And the N 1s signals can be deconvoluted into four types of nitrogen species as shown in Fig. 3(c): pyridinic nitrogen at the binding energy of ~398.4 eV (N1), pyrrolic nitrogen at ~399.8 eV (N2), graphitic nitrogen at ~401.0 eV (N3), and oxidized nitrogen at ~402.9 eV (N4) [23]. The relative content for each type is demonstrated in Fig. 3(d). The percentage of pyridinic-N (N1) and graphitic-N (N3) is 32.85% and 18.01%, respectively.

Fig. 3(e) shows an HAADF-STEM image of the N-MHC, displaying the formation of honeycomb-like structures. To determine the distribution of nitrogen in the N-MHC, elemental identification is performed. It shows the energy dispersive X-ray (EDX) maps for carbon, nitrogen and oxygen based on the region shown in the HAADF image on the left. The C, N, O maps match well, indicating that nitrogen is homogeneously distributed throughout N-MHC.

In addition, the weight loss of MHC after NH₃ pyrolysis process is recorded as 15.7%, whereas the value obtained from blank

experiment in Ar atmosphere is just 8.3%. The loss in Ar atmosphere may be from further carbonization of MHC, or from the decomposition of surface oxygen containing functional groups. However, the enlarged loss in NH₃ should be from an etching action on carbon by NH₃. As previously studied, oxygen containing functional groups were found responsible for reactions with NH₃ and C–N bond formation, and the NH₃ activation involve the replacement of oxygen-bearing species by nitrogen-containing groups on the carbon [24]. And specifically, the incorporation of nitrogen is accompanied by the decrease of oxygen content, seen from the result in Fig. 3(b), that the relative intensity of oxygen in N-MHC is lower than MHC (from 5.42 to 3.66 at.% of oxygen). Thus, simultaneous nitrogenation and deoxygenation are realized.

The effect of nitrogen doping on N-MHC was also studied by Raman spectroscopy. According to Fig. 3(f), two distinct peaks corresponding to D and G bands are observed at approximately 1346 cm⁻¹ and 1588 cm⁻¹ for both samples, respectively. The D

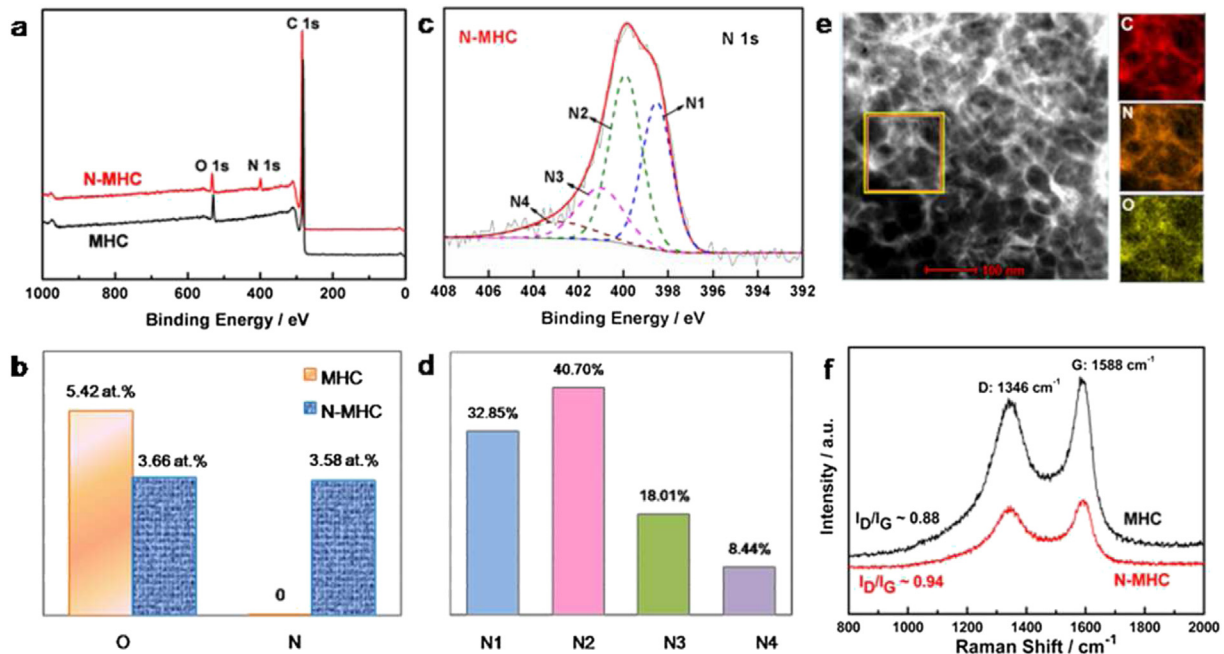


Fig. 3. Structural and compositional characterization of N-MHC and MHC materials. (a) XPS survey spectra for N-MHC and MHC, (b) Chart showing the percentages (in atom %) of oxygen and nitrogen in the N-MHC and MHC material measured by XPS. (c) The N 1s fitting spectra and (d) the corresponding ratio for N-MHC. (e) High-angle annular dark-field (HAADF)-scanning transmission electron microscopy (STEM) image of N-MHC, and C, N, O element maps of N-MHC. (f) Raman spectra for N-MHC and MHC.

bands are assigned to the disorder structure on the graphitic plane, and the G bands are attributed to the E_{2g} vibrational mode in the sp^2 -bonded graphitic carbons. The relative intensities of these two peaks reflect the degree of disorder. The calculated intensity ratio of D band to G band (I_D/I_G) for MHC and N-MHC are

0.88 and 0.94, respectively. It suggests that N-MHC possesses more defects.

The ORR catalytic activities for carbon materials were investigated through electrochemical cyclic voltammetry (CV) tests. As shown in Fig. 4(a), relative to the MHC material, a significant

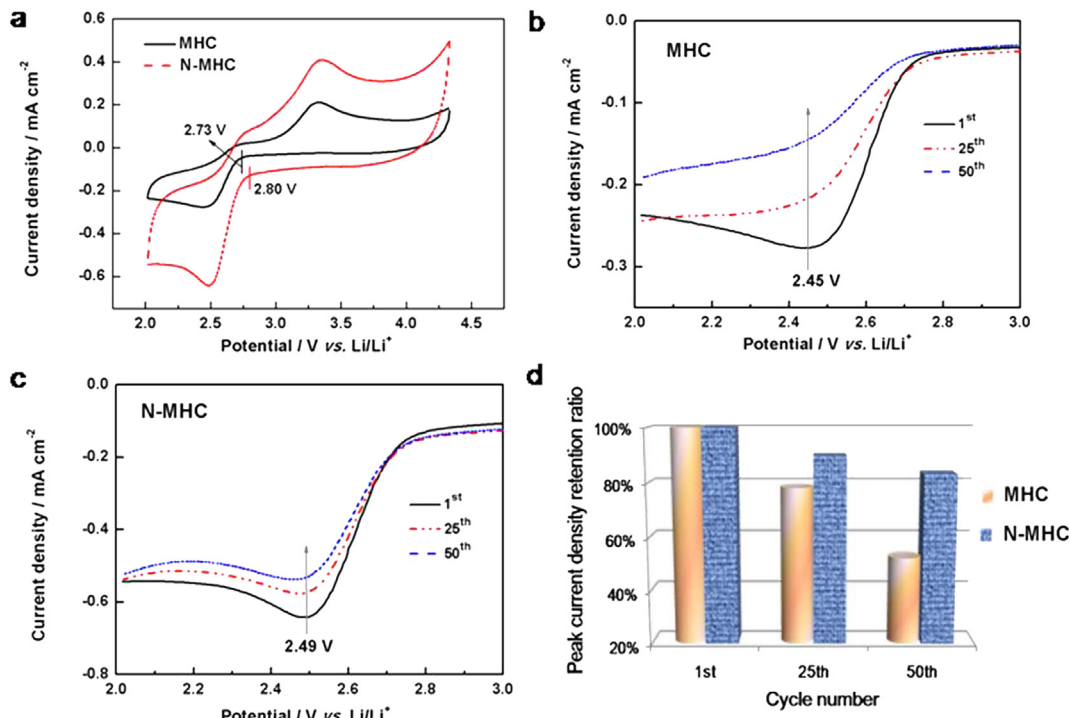


Fig. 4. (a) CV curves of MHC and N-MHC. Cycling stability tests of (b) MHC and (c) N-MHC. Electrolyte: O_2 -saturated 0.5 M bis(trifluoromethane)sulfonamide lithium (LiTFSI) in tetraethylene glycol dimethyl ether (TEGDME) solution. $t = 25$ °C. Scan rate: 10 mV s⁻¹. Carbon composition: loading for MHC and N-MHC were 77 $\mu\text{g cm}^{-2}$. (d) Peak current density retention ratio after 25 and 50 cycles for N-MHC and MHC, respectively.

improvement in activity is observed for N-MHC, as evidenced by positive shifts in pristine ORR onset potential. Moreover, the ORR peak current density is increased by about 2.3 times ($-0.642 \text{ mA cm}^{-2}$ vs. $-0.277 \text{ mA cm}^{-2}$), as shown in Fig. 4(b) and (c). These results reveal that the N-MHC displays better ORR activity, in accordance with the anticipation based on the above physical and chemical characterizations with the synthesized materials. In addition to the improved surface area and pore volume for N-MHC, the ORR activity is actually mainly determined by the surface chemical composition. It is clear that the N-MHC sample contains both pyridinic-N (N1) and graphitic-N (N3). Recent study suggests that the pyridinic type nitrogen is generally considered to be responsible for the ORR active sites in fuel cells and graphitic type nitrogen for promoting the limiting current density [25]. Nitrogen functionalities introduce active sites that could participate in breaking the O–O bonds of oxygen molecules. However, in non-aqueous environment, a definite understanding of the mechanism of nitrogen bonding configuration on ORR activity still needs more detailed investigations, although the nitrogen doping strategy has been well proved.

The stability of the cathode is another key parameter for LOB. The cycling ability of N-MHC and MHC were studied and compared in Fig. 4(d). As shown in Fig. 4(b) and (c), the ORR curve remains the same shape after 50 cycles for N-MHC sample; however, it declines obviously for MHC just after 25 cycles. As shown in Fig. 4(d), after 50 cycles, a higher retention ratio (83.3%) of peak current density is obtained for N-MHC, while it is 52.3% for MHC. N-MHC displayed more stable cycling ability after ammonia activation. Previous findings has shown that oxygen-containing carbon promotes electrolyte decomposition during discharge and charge in a Li–O₂ cell, giving rise to undecomposed side products such as Li₂CO₃ and lithium carboxylates. This would result in the decrease of active area for electrode reaction as well as the capacity fade. Furthermore, the reactions between oxygen containing groups and intermediate radicals will make the situation more severe [26]. With ammonia modification, a more stable reaction interface can be achieved by nitrogen species substitution for oxygen-containing groups, indicated by XPS analysis. This would propose an effective strategy working for enhanced cycling performance in LOBs, that is to remove or replace unstable oxygen containing groups through the formation

of more stable C-M groups (M related to other components) on carbon material.

As shown in Fig. 5, the N-MHC electrode delivers an initial discharge capacity of 12,600 mAh g⁻¹, and 6000 mAh g⁻¹ for MHC. Based on the result in previous work that was obtained under the same experiment conditions, the capacity for N-MHC cathode is 4 times that of the best commercial carbon-Ketjenblack [13]. The total pore volume of N-MHC increased 40% (from 1.10 to 1.55 cm³ g⁻¹), while the N-MHC cathode shows a capacity twice as that of the MHC. Thus super high capacity could be attributed to oxygen transport enhancement from the increased inner large holes. Moreover, the N-MHC cathode exhibits higher average discharge plateau about 40 mV than MHC (2.75 V vs. 2.71 V). The higher discharge voltages with N-MHC could be partially from improved ORR activity by nitrogen functionalities, and partially from faster lithium and oxygen transport in enlarged pore structure.

4. Conclusions

In the present work, nitrogen-doped hierarchically carbon material is obtained after NH₃ activation. The activation effect on surface modification realizes nitrogen doping, simultaneously, its effect on mesopores etching leads to the construction of intrinsic macroporous holes, which can act as the local O₂ buffering “caves” and transport “highways”. The superior discharge capacity (12,600 mAh g⁻¹) and increased ORR activity indicate that N-MHC can be promising candidates as cathode material for LOBs. In addition, the strategy of the replacement of O containing groups by more stable N containing groups is provided in a new light to improve carbon stability for LOBs. Meanwhile, the novel features of N-MHC are expected to find broad applications in other energy storage devices such as lithium–sulfur batteries, supercapacitors, etc.

Acknowledgments

The authors thank Haisheng Wei and Baoshan Wu for the help with the thermogravimetry test and schematic drawing.

References

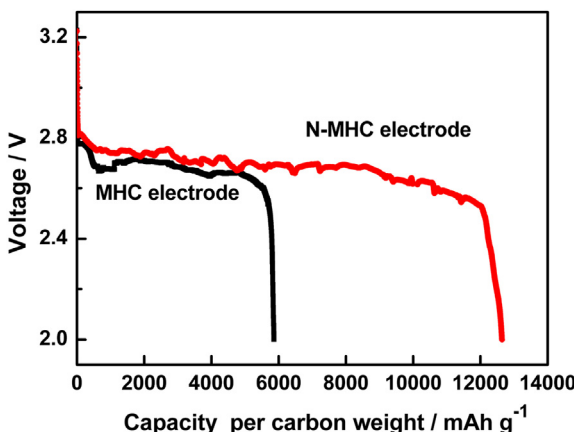


Fig. 5. Li–O₂ single cell discharge voltage curves with MHC and N-MHC as cathodes, respectively. Cathode: 15 mm in diameter. Carbon loading: $6.3 \pm 0.4 \text{ mg}$. Electrolyte: 1.0 M LiTFSI in TEGDME. Separator: a polypropylene fiber separator (Novatexx 2471, Freudenberg Filtration Technologies KG, 22 mm in diameter). Anode: Li foil (16 mm in diameter, 0.45 mm thick). Operating conditions: $P_{O_2} = 1.2 \text{ atm}$, $I = 30 \text{ mA g}^{-1}$ carbon (ca. 0.1 mA cm^{-2}), $t = 25^\circ\text{C}$.

- [1] K.M. Abraham, Z. Jiang, J. Electrochem. Soc. 143 (1996) 1–5.
- [2] R.R. Mitchell, B.M. Gallant, C.V. Thompson, Y. Shao-Horn, Energy Environ. Sci. 4 (2011) 2952–2958.
- [3] R. Black, S.H. Oh, J.-H. Lee, T. Yim, B. Adams, L.F. Nazar, J. Am. Chem. Soc. 134 (2012) 2902–2905.
- [4] J. Xiao, D.H. Wang, W. Xu, D.Y. Wang, R.E. Williford, J. Liu, J.G. Zhang, J. Electrochem. Soc. 157 (2010) A487–A492.
- [5] X. Ren, S.S. Zhang, D.T. Tran, J. Read, J. Mater. Chem. 21 (2011) 10118–10125.
- [6] C. Tran, X.Q. Yang, D.Y. Qu, J. Power Sources 195 (2010) 2057–2063.
- [7] X.H. Yang, P. He, Y.Y. Xia, Electrochim. Commun. 11 (2009) 1127–1130.
- [8] X. Lin, L. Zhou, T. Huang, A. Yu, J. Mater. Chem. A 1 (2013) 1239.
- [9] Y. Cui, Z. Wen, X. Liang, Y. Lu, J. Jin, M. Wu, X. Wu, Energy Environ. Sci. 5 (2012) 7893.
- [10] T. Zhang, H. Zhou, Angew. Chem. Int. Ed. 51 (2012) 11062–11067.
- [11] Z.L. Wang, D. Xu, J.J. Xu, L.L. Zhang, X.B. Zhang, Adv. Funct. Mater. 22 (2012) 3699–3705.
- [12] J. Xiao, D. Mei, X. Li, W. Xu, D. Wang, G.L. Graff, W.D. Bennett, Z. Nie, L.V. Saraf, I.A. Aksay, J. Liu, J.-G. Zhang, Nano Lett. 11 (2011) 5071–5078.
- [13] J. Li, H. Zhang, Y. Zhang, M. Wang, F. Zhang, H. Nie, Nanoscale 5 (2013) 4647–4651.
- [14] Y. Li, J. Wang, X. Li, J. Liu, D. Geng, J. Yang, R. Li, X. Sun, Electrochim. Commun. 13 (2011) 668–672.
- [15] Y. Li, J. Wang, X. Li, D. Geng, M.N. Banis, R. Li, X. Sun, Electrochim. Commun. 18 (2012) 12–15.
- [16] H. Nie, H. Zhang, Y. Zhang, T. Liu, J. Li, Q. Lai, Nanoscale 5 (2013) 8484–8487.
- [17] G. Wu, N.H. Mack, W. Gao, S. Ma, R. Zhong, J. Han, J.K. Baldwin, P. Zelenay, ACS Nano 6 (2012) 9764–9776.
- [18] W. Shen, W. Fan, J. Mater. Chem. A 1 (2013) 999.
- [19] B. Stöhr, H. Boehm, R. Schlögl, Carbon 29 (1991) 707–720.

- [20] X. Wang, J.S. Lee, Q. Zhu, J. Liu, Y. Wang, S. Dai, *Chem. Mater.* 22 (2010) 2178–2180.
- [21] C.L. Mangun, K.R. Benak, J. Economy, K.L. Foster, *Carbon* 39 (2001) 1809–1820.
- [22] C. Zhao, W. Wang, Z. Yu, H. Zhang, A. Wang, Y. Yang, *J. Mater. Chem.* 20 (2010) 976.
- [23] P. Matter, L. Zhang, U. Ozkan, *J. Catal.* 239 (2006) 83–96.
- [24] X. Li, H. Wang, J.T. Robinson, H. Sanchez, G. Diankov, H. Dai, *J. Am. Chem. Soc.* 131 (2009) 15939–15944.
- [25] L. Lai, J.R. Potts, D. Zhan, L. Wang, C.K. Poh, C. Tang, H. Gong, Z. Shen, J. Lin, R.S. Ruoff, *Energy Environ. Sci.* 5 (2012) 7936–7942.
- [26] M.M. Ottakam Thotiyil, S.A. Freunberger, Z. Peng, P.G. Bruce, *J. Am. Chem. Soc.* 135 (2013) 494–500.